Two-Point Shear Correlations as Probes of Large-Scale Structure in the CFHTLS Wide Fields

Sean Pike, Ian Dell'Antonio

Abstract

We present weighted and calibrated two-point shear correlation functions $\xi_{\pm}(\theta)$ calculated in five redshift bins across the four Canada-France-Hawaii Telescope Legacy Survey Wide fields, W1, W2, W3, and W4, using data processed by the CFHT Lensing Survey specifically for use in weak-lensing studies. We report an excess correlation of order 10^{-4} at an angular separation $\theta = 0.015$ degrees, which drops to zero as the angular separation increases. In addition, we find that in general as redshift increases, excess correlation also increases. Correlation functions calculated in the nearest redshift bin do not follow this trend, but we argue that this is due to inaccurate redshift binning as a result of imprecise Bayesian redshift estimation. Overall, these findings are in agreement with past studies of weak lensing by large-scale structure. As such, the correlation functions produced may be robust enough for use in further cosmological studies, but require more rigorous analysis before use.

Introduction

The distortion of spacetime due to the presence of mass results in a deflection of the otherwise straight paths by which light travels. Thus images of distant objects, which lie behind large distributions of matter, appear distorted in an effect dubbed gravitational lensing. While some lensing effects, such as those due to a black hole, are dramatic, most lensing involves only very slight distortion which is impossible to observe with the naked eye. This effect, called weak lensing, can however be observed via statistical analysis of large numbers of galaxies and has proven to be a powerful cosmological probe. Because gravitational lensing observations contain information regarding the mass distribution, largely made up of dark matter, between the observer and the observed object, they can be used to determine various characteristics of dark matter. For example, dark matter halos around galaxies can be investigated by measuring galaxy-galaxy lensing, or the distortion of galaxies caused by less distant ones. In addition, by analyzing the distortions of galaxies which lie behind galaxy clusters, the radial density profiles of these clusters can be estimated. Tracing the evolution of cluster mass profiles in turn can provide estimates of various cosmological parameters (Wittman et al., 2009).

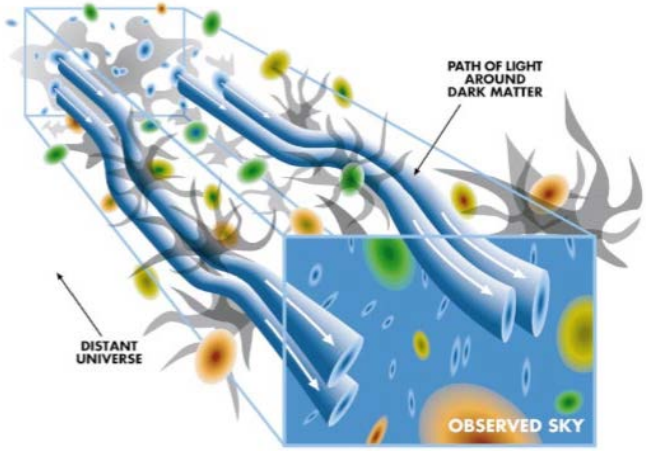

Figure 1: When light from a distant galaxy passes through a gravitational potential, its path is deflected resulting in a distortion in the observed image. Because light from galaxies which appear close to one another on the night sky passed through similar potentials, the images of these galaxies are similarly distorted, resulting in an excess correlation of galaxy shapes at small angular separations. (Wittman, D.M. et al., 2000)

While the growth of over-densities in the nonlinear regime often requires the use of N-body simulations to analyze and predict, weak gravitational lensing by large-scale structure, or cosmic shear, provides a direct probe of nonlinear perturbations in dark matter

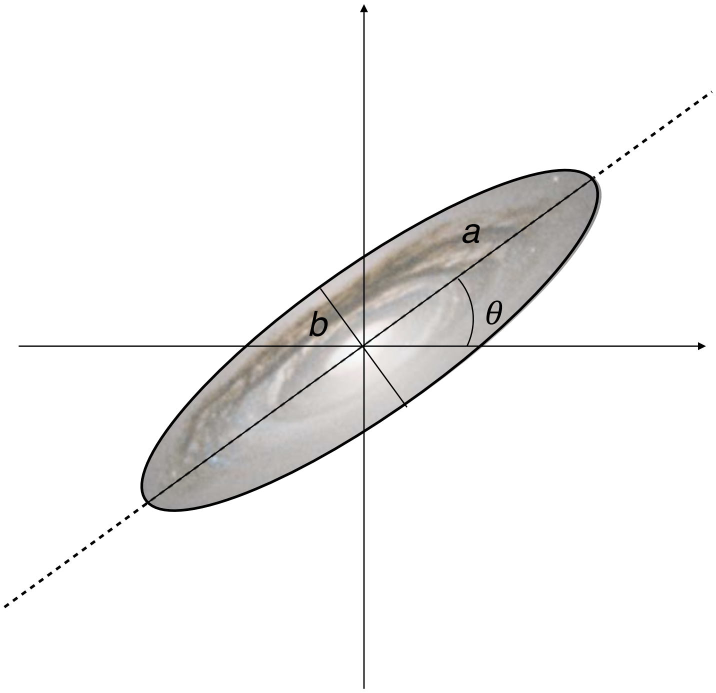

Figure 2: A galaxy's image is approximated as an ellipse with semi-major axis *a* and semi-minor axis *b*. It is oriented at an angle θ measured counterclockwise from the horizontal axis.

distributions. By analyzing the effects of cosmic shear over large areas of the sky, one may determine average characteristics of large-scale structure. Weak lensing by large-scale structure was first observed at the beginning of the 21st century (Van Waerbeke et al., 2000), and has since been utilized to map distributions of dark matter (Clowe et al., 2004; Van Waerbeke et al., 2012) as well as to constrain cosmological parameters such as the matter energy density, Ω_m, and the amplitude of the linear power spectrum, σ_8 (Hoekstra et al., 2002; Fu et al., 2008; Semboloni et al., 2011). Here we attempt to characterize weak lensing by large-scale structure as well as its evolution in the CFHTLS Wide fields using the two-point correlation functions, $\xi_\pm$.

The shape of a galaxy's image can be approximated as an ellipse and is therefore described by its ellipticity, ϵ, a complex quantity with components ϵ_1 and ϵ_2 such that $\epsilon = \epsilon_1 + i\epsilon_2$ and where ϵ_1 and ϵ_2 are given by

$$\epsilon_1 = \frac{a-b}{a+b}\cos 2\theta \qquad (1)$$

$$\epsilon_2 = \frac{a-b}{a+b}\sin 2\theta. \qquad (2)$$

Here, *a* and *b* are the semi major and semi minor axes of the ellipse, respectively, and θ is the orientation angle of the ellipse measured counterclockwise from the horizontal axis (Heymans et al, 2012), as shown in Figure 2. In addition, the complex ellipticity can be written as a function of a galaxy's intrinsic ellipticity and the shear of the galaxy. When a galaxy's intrinsic ellipticity, ϵ_0, is much larger than its shear, γ, and the observed ellipticity is small compared to unity, this function simplifies to a simple sum of the intrinsic shape and the shear. In other words, in the absence of gravitational lensing, a galaxy would appear to have ellipticity ϵ_0. The gravitational potential which light from the galaxy experiences on its way to an observer then stretches the image of the galaxy slightly, adding a small complex shear γ so that

$$\epsilon = \epsilon_0 + \gamma. \qquad (3)$$

Thus the shear of a galaxy's image reveals information regarding the mass distribution between the galaxy and the observer. However, there is no way to know, a priori, the contributions to the observed shape of shear and intrinsic ellipticity when looking at a single galaxy. Therefore it is useful to compare the shapes of a large number of galaxies.

Consider two galaxies labelled *i* and *j*. If the light from these galaxies passes through similar gravitational potentials, then it follows that the images observed will be similarly distorted. In other words, the shears γ_i and γ_j will be oriented in approximately the same direction so that $\gamma_i \,/\, |\gamma_i| \approx \gamma_j \,/\, |\gamma_j|$. Thus, the correlation between the observed ellipticities of the two galaxies will be slightly larger than that of the intrinsic ellipticities, which on average are uncorrelated. While (in the case of weak lensing) this increase in correlation is impossible to observe for just two galaxies due to the fact that the shear contribution is much smaller than the intrinsic ellipticities, the effect is evident when correlating the shapes of large numbers of galaxies. To achieve this, we may define two correlation functions, ξ_+ and ξ_-, such that

$$\xi_\pm(\theta) = \langle \gamma_t \gamma_t \rangle \pm \langle \gamma_x \gamma_x \rangle \qquad (4)$$

Where $\langle \gamma_{t,x} \;\; \gamma_{t,x} \rangle$ is the mean value of the product of the tangential and cross-components, respectively, of the shears of two galaxies separated on the night sky by angle θ (Schneider et al, 2002). These are defined as the components of the shear rotated into the frame in which the x-axis is the line connecting the centers of the two galaxies being compared. In other words, if in this frame a galaxy with shear γ is oriented at an angle ϕ with respect to the x-axis, then the tangential and cross-components are given by

$$\gamma_t = |\gamma| \cos 2\phi \qquad (5)$$

and

$$\gamma_x = |\gamma| \sin 2\phi. \qquad (6)$$

Although it can be shown (see Hoekstra et al, 2002; Schneider et al, 2002; Miralda-Escudé, 1991) that the correlation functions, $\xi_\pm(\theta)$, are directly related to the power spectrum, matter energy density, and aperture mass statistic, these functions may not be determined directly from observation for it is not possible to directly measure the shear of an image due to the intrinsic ellipticity. However we may use the fact that for no intrinsic alignment of galaxies,

$$\langle \gamma_{t,x}\, \gamma_{t,x} \rangle \approx \langle \epsilon_{t,x}\, \epsilon_{t,x} \rangle \ , \qquad (7)$$

in order to approximate the two-point correlation functions:

$$\xi_\pm(\theta) \approx \langle \epsilon_t\, \epsilon_t \rangle \ \pm \ \langle \epsilon_x\, \epsilon_x \rangle \qquad (8)$$

which is observable. Thus, by measuring the shapes of galaxies and determining their correlation, one may constrain cosmological parameters and gain insight into the distribution of dark matter. In addition, by binning galaxies according to redshift and correlating shapes only within these bins, one may also determine how the distribution of dark matter has changed as large scale structure has evolved over time.

Data

All data we used was obtained from the Canada-France-Hawaii Lensing Survey (Heymans et al. 2012), hereafter referred to as CFHTLenS. The CFHTLenS survey analysis combined weak lensing data processing with THELI (Erben et al. 2012), Bayesian shear measurement with the *lens*fit algorithm (Miller et al. 2012), and photometric redshift measurement with PSF-matched photometry (Hildebrandt et al. 2012). A full

Wide field	RA of Center (J2000)	DEC of Center (J2000)	Total Area (deg^2)	Filters
W1	2:18:00	-07:00:00	63.75	u^*, *g, r, i/y, z*
W2	08:57:49	-03:19:00	22.56	u^*, *g, r, i/y, z*
W3	14:17:54	+54:30:31	44.22	u^*, *g, r, i/y, z*
W4	22:13:18	+01:19:00	23.3	u^*, *g, r, i/y, z*

Table 1: Summary of the CFHTLS Wide fields. (Goranova et al. 2009)

Filter	Mean number of exposures	Mean exposure time (s)	Mean limiting magnitude	Mean seeing (arc seconds)
u^*	5	3000	25.34	0.850
g	5	2500	25.47	0.780
r	4	2000	24.82	0.720
i/y	7	4300	24.48	0.640
z	6	3600	23.60	0.680

Table 2: Summary of the filters used in the CFHTLS T0006 data release. Note that shapes were estimated using data from the i/y filter. The mean seeing is the mean full-width half-mass of stellar sources and the mean limiting magnitude is corresponds to the 50% completeness limit for a point-like source (Goranova et al. 2009). A more detailed synopsis of fields and filters used in the CFHTLS can be found at http://terapix.iap.fr/cplt/table_syn_T0006.html

systematic error analysis of the shear measurements in combination with the photometric redshifts is presented in Heymans et al. (2012), with additional error analyses of the photometric redshift measurements presented in Benjamin et al. (2012).

Data originates from release T0006 of the Canada-France-Hawaii Telescope Legacy Survey (CFHTLS), which consists of images obtained by MegaPrime/MegaCam. This release is described in detail by Goranova et al. (2009). The four wide fields, W1, W2, W3, and W4 were then further analyzed by the CFHTLenS team in order to produce data which is suitable for weak lensing studies. This process, which is detailed by Heymans et al. (2012), includes, in addition to the analysis described above, flagging defects, masking objects which are unusable, distinguishing stars from galaxies, and assigning weights to objects based on the precision of their shape measurements. Figures 3 and 4 show the

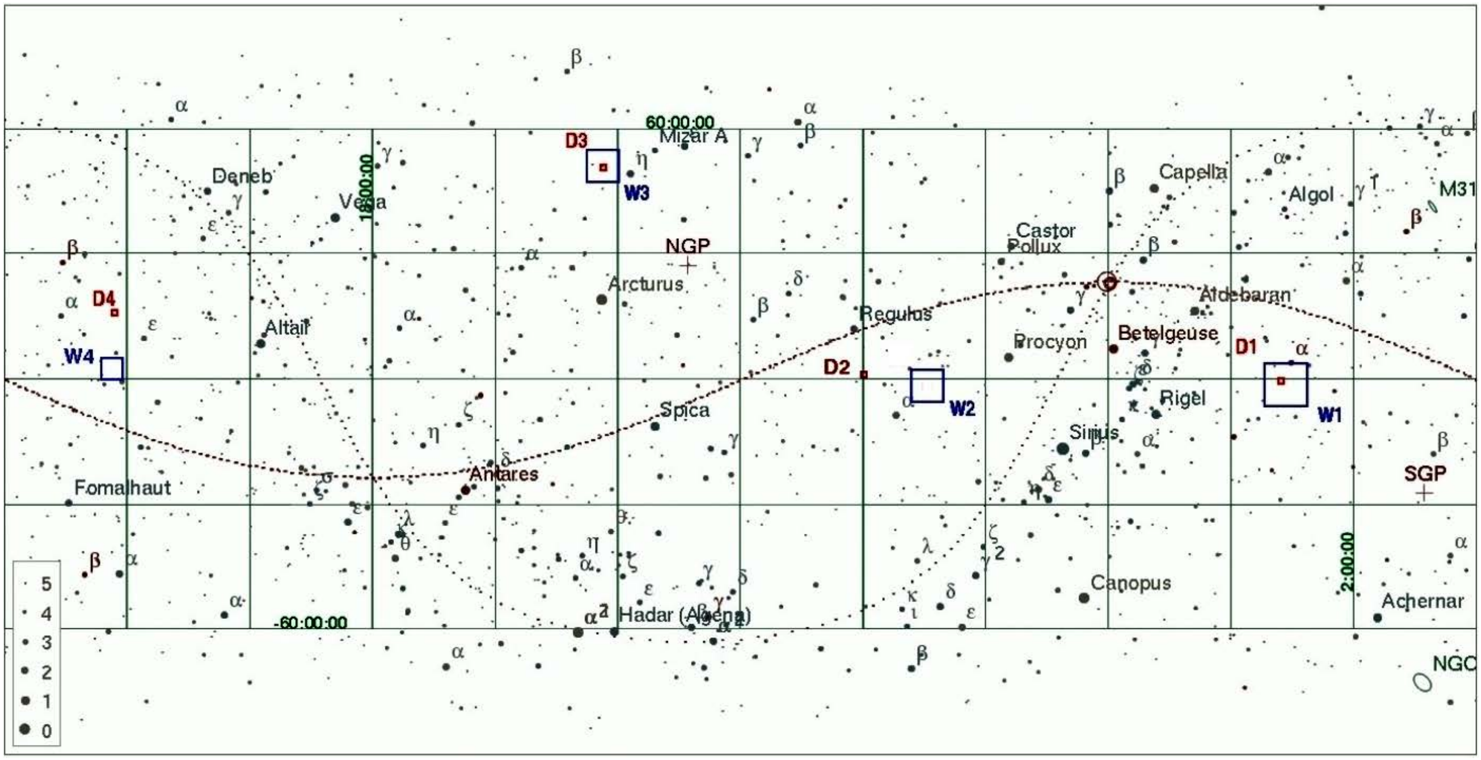

Figure 3: The position and approximate size of each CFHTLS-Wide field as seen on the sky. (Goranova et al. 2009)

positions of the CFHTLS Wide fields on the sky as well as the area spanned by each, and Table 1 provides a summary of each Wide field. Combined, the Wide fields cover approximately 154 square degrees.

As is the case with all astronomical data, error was introduced to the data by imperfections in the CCDs, varying pointing and focus of the telescope, artifacts such as cosmic rays, and atmospheric effects. These combine to produce anisotropies in the Pixel Spread Function, or PSF. This is a function which describes how a point source of light appears when observed via a given apparatus. The point source may be distorted or dispersed, resulting in an observed shape which does not accurately reflect the actual shape of the object or its shear. Because the CFHTLenS catalogs contain data from many exposures pointing at various points in the sky, the PSF varies by location. Thus, the shapes of galaxies contain contributions which are not related to gravitational lensing. These effects will introduce error to the correlation

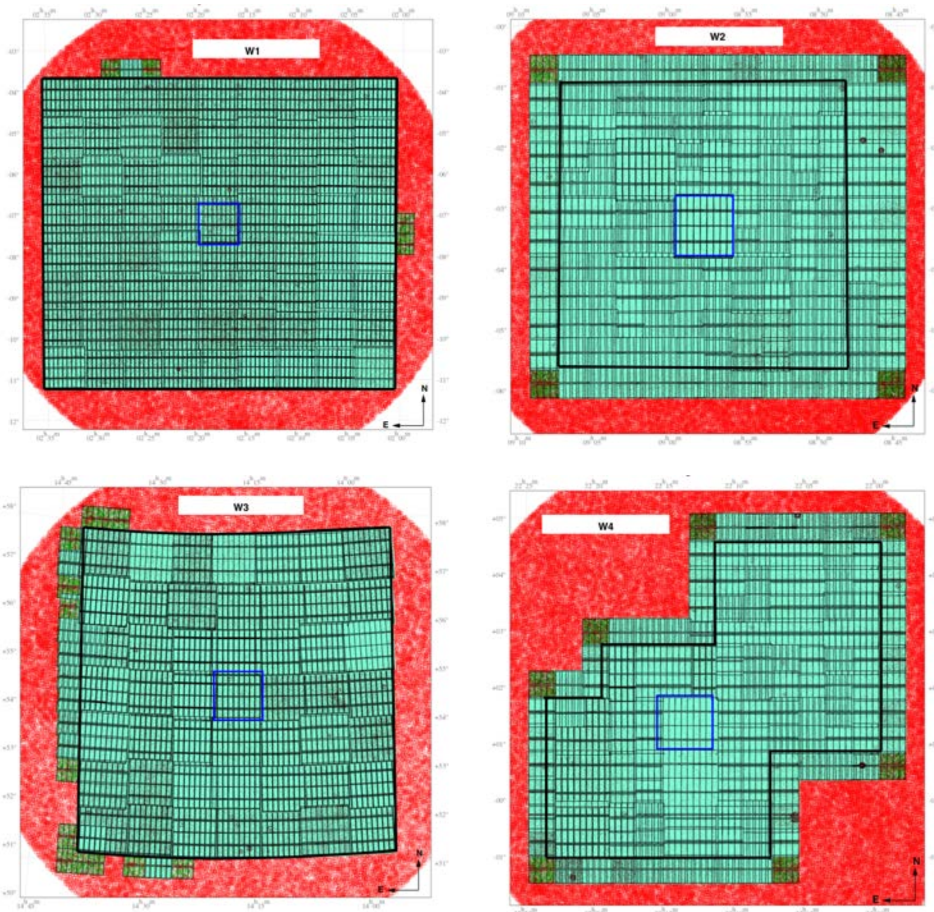

Figure 4: The shapes of the CFHTLS-Wide fields vary. The area shaded in green is the data observed by the MegaCam and the data outlined by the thick black line is the area included in the CFHTLS release. W1 covers ~63.8 square degrees, W2 covers ~22.6 square degrees, W3 covers ~44.2 square degrees, and W4 covers ~23.3 square degrees for a total coverage of approximately 154 square degrees. (Goranova et al. 2009)

functions, so they must be accounted for. During the processing of the CFHTLenS data, image distortion was removed from galaxy shape data by determining the PSF at the positions of stars. Because stars have no intrinsic ellipticity and those that can be observed are too close to Earth to be lensed, they are perfect test point sources. Their distortions were used to estimate the value of the PSF at discrete locations. Next, the PSF was interpolated by a third-order polynomial so that the value of the PSF at the positions of galaxies could be estimated (Miller et al. 2012). These effects were then corrected for in estimations of the shapes of galaxies. In addition to distortions due to physical imperfections involved in observation, there is bias introduced to the shapes of galaxies due

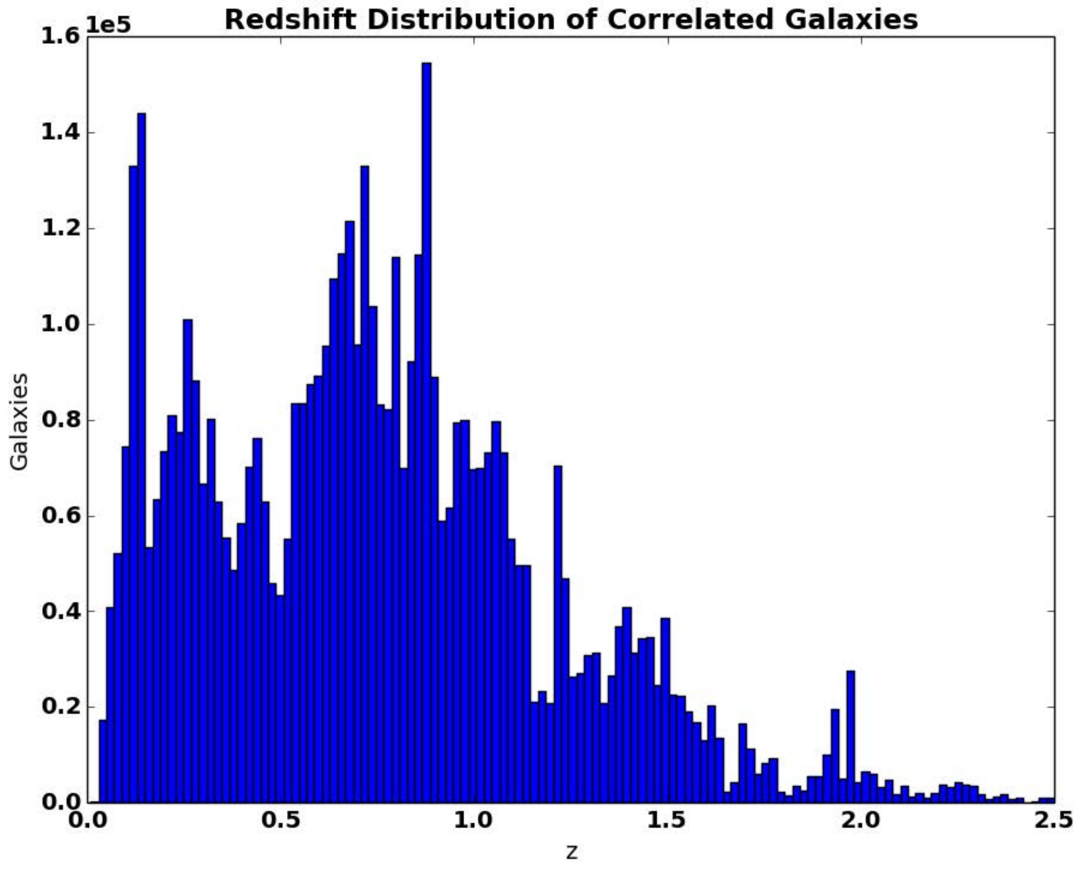

Figure 5: Distribution of galaxies by redshift. Galaxies are abundant below z=1.0, but the population sharply drops off as z increases. In addition, the region $0.5 < z < 1.0$ is clearly the most densely populated. This irregular distribution illustrates the need for irregular redshift binning when computing the correlation functions.

to the Bayesian estimation technique, which depends on prior knowledge and models chosen by Miller et al (2012). While Miller et al. detect this bias, they do not not provide a conclusive source. However, they offer hypotheses, such as errors in the PSF models used or possible accuracy bias between large and small galaxies. In order to counteract this bias, calibration terms, m, a multiplicative term which is a function of size and signal to noise ratio, and $\boldsymbol{c}$, an additive term which has components parallel to ϵ_1 and ϵ_2 and is dependent on the PSF value at the position of each galaxy, are provided in the data catalogues. Their effect on the observed ellipticity is given by equation 8 (Heymans et al. 2012):

$$\epsilon_{obs} = (1+m)[\gamma + \epsilon_{int}] + \boldsymbol{c} \qquad (9)$$

Thus ***c*** should be subtracted from the observed ellipticities, and observed ellipticities must also be divided by $1+m$.

Redshift values too were calculated using a Bayesian approach, meaning that the value assigned to each galaxy is the peak of a likelihood function calculated using the Bayesian Photometric Code detailed by Benítez (1999) and priors and template galaxy sets given by Hildebrandt et al. (2012).

Methods

Weighted two-point shear correlation functions, $\xi_\pm(\theta)$, were produced for angular separations $\theta < 1.5$ degrees within five redshift bins of varying size. Correlations were calculated within W1, W2, W3, and W4 (such that the pairs of galaxies in Equation 8 are always within the same Wide field, but the averages in Equation 8 are calculated over pairs within all four fields). This required iterating over 9.28×10^{11} pairs of galaxies even after galaxies were separated by Wide field and by redshift. Note that although 9.28×10^{11} pairs of galaxies were iterated over, the majority of these pairs have separations greater than 1.5 degrees and therefore do not contribute to the correlation functions.

In order to produce the functions, unusable data was removed from the raw CFHTLenS Wide field catalogs. This includes objects which were assigned a mask value greater than one and objects which lie in fields deemed by Heymans et al. (2012) to be too noisy for scientific use. In addition objects with weights equal to zero were removed as they do not contribute to the correlation functions. Galaxies and stars were then separated using the star_flag value provided in the catalogs, which, according to CFHTLenS data product documentation (Hildebrandt 2012), gives an almost perfectly complete galaxy sample by classifying objects based on size and color. The raw catalogues contain data for almost 22 million galaxies. After removing masked, zero-weight, and bad field galaxies, 5,464,351 usable galaxies remained in the four fields.

Next, galaxies were separated into five redshift bins of varying width such that the bins have redshift boundaries, $0 < z <= 0.3$,

$0.3 < z <= 0.6$, $0.6 < z <= 0.8$, $0.8 < z <= 1.1$, and $1.1 < z <= 2.5$. Bin widths and boundaries were chosen such that each bin contains around the same number of galaxies. The unweighted average number of galaxies in each bin is 1,072,285, and the largest deviation from the mean is 13.8%. Figure 5 shows the redshift distribution of galaxies used in correlation.

It is important to note that galaxies were binned according to the Bayesian redshift estimate provided in the CFHTLenS catalogues and, as such, binning is not perfectly precise. The method by which the redshifts were estimated produces a likelihood function, the peak of which is reported as a galaxy's photometric redshift (Benítez, N., 1999). This likelihood has a finite width however, meaning that there is a maximum redshift, z_{max}, and a minimum redshift, z_{min}, between which the galaxy's actual redshift may lie. Thus redshift bins may overlap near their boundaries. The distribution of z_{max}- z_{min} in each redshift bin is shown in Figure A1. It is clear from these distributions that there are a significant number of galaxies whose redshift likelihood functions have widths comparable to or larger than the width of the redshift bin in which they have been placed according to their reported photometric redshift. This poses potential problems as there is no information to be gained from correlating galaxies in redshift bins with poorly defined, overlapping boundaries. However, testing of the BPZ method by Benítez (1999) as well as Hildebrandt et al. (2012) shows that for galaxies whose redshift has been measured spectroscopically, the Bayesian estimate agrees very well with the spectroscopic redshift: Benítez reports a root mean square error, $\Delta z \approx 0.06(1 + z_{spec})$, which is well within the widths of our redshift bins. Although this does not provide perfect confidence in the widths of our redshift bins, it at least ensures that correlating in these bins will provide a meaningful result.

After galaxies were separated into redshift bins, the weighted products of ellipticities were determined for each pair of galaxies separated by less than 1.5 degrees and which lie within the same Wide field and redshift bin. When calculating small angular separations, the curvature of the sky may be ignored, but at separations of order unity and greater this curvature contributes to the separation. Thus, angular distances between galaxies were calculated as the separation on the surface of a sphere using the following equation (Fu et al. 2008):

$$\cos\theta = \cos(\alpha_i - \alpha_j)\cos\delta_i\cos\delta_j + \sin\delta_i\sin\delta_j \qquad (10)$$

Where θ is the angular separation between a pair of galaxies labelled *i* and *j*, α_i and α_j are the right ascensions of the galaxies, and δ_i and δ_j are the declinations of the galaxies. It is also necessary to account for the curvature of the sky when determining the tangential and radial ellipticity components in a given galaxy-pair coordinate frame. Fu et al. (2008) also provide a relationship between the positions of the two galaxies which define the rotated coordinate frame and the angle the frame makes with the horizontal:

$$tan\varphi = \frac{sin(\alpha_i - \alpha_j)cos\delta_j}{cos\delta_i sin\delta_j - sin\delta_i cos\delta_j cos(\alpha_i - \alpha_j)} \qquad (11)$$

where φ is the angle of the rotated coordinate frame.

Next, the weighted products of ellipticities are defined as $w_i w_j(\epsilon_{it}\ \epsilon_{jt})$ and $w_i w_j(\epsilon_{ir}\ \epsilon_{jr})$ where w_i and w_j are the weights assigned to galaxies *i* and *j* respectively by the CFHTLenS pipeline. Given this definition, the weighted correlation functions are defined as

$$\xi_{\pm}(\theta) = \frac{\sum_{i,j} w_i w_j(\epsilon_{it}\epsilon_{jt} \pm \epsilon_{ir}\epsilon_{ir})}{\sum_{i,j} w_i w_j} \qquad (12)$$

where sums are over pairs of galaxies separated by $\theta \pm \Delta\theta$ degrees. $\Delta\theta$, or the angular bin width, was chosen to be 0.015 degrees, meaning that each correlation function consists of 50 values, one for each angular separation bin.

The additive calibration constants were subtracted from each ellipticity value individually before rotating the given values ϵ_1 and ϵ_2 into the frame defined by the line connecting the galaxies. Multiplicative calibrations were applied via a weighted ensemble correction. This method is recommended by Miller et al. (2012) in order to avoid error due to cases when 1+*m* approaches 0. For each separation bin, a calibration term $K(\theta)$ was determined. This term is defined by Miller et al. (2012) as

$$1+K(\theta) = \frac{\sum_{i,\,j} w_i w_j (1+m_i)(1+m_j)}{\sum_{i,\,j} w_i w_j} \qquad (13)$$

The final calibrated result is then given by

$$\xi_{\pm}^{cal}(\theta) = \frac{\xi_{\pm}(\theta)}{1+K(\theta)} \qquad (14)$$

Appendix C contains the code used to calculate these functions within a single Wide field. In order to determine the total correlation functions taken over W1, W2, W3, and W4, the individual calibrated functions of each field were multiplied by their corresponding $1+K(\theta)$ function and the sum of the products of weights. These were then added together to obtain the sum which appears in the numerator of Equation 12 over all four fields. The individual $1+K(\theta)$ functions were also multiplied by the sum of products of weights and added to obtain the sum in the numerator of Equation 13 over all four fields. Finally, the total uncalibrated correlation functions were divided by the total $1+K(\theta)$ functions in order to obtain the final calibrated correlation functions taken over W1, W2, W3, and W4.

Error in the correlation functions was estimated using the equation described by Miralda-Escudé (1991):

$$\langle(\Delta\xi_{\pm})^2\rangle^{1/2} = \frac{\sigma_{\epsilon}^2}{n_g(2\pi\theta\Delta\theta\omega)^{1/2}} \qquad (15)$$

Where σ_ϵ is the average square of the ellipticities of all galaxies in the redshift bin being correlated, n_g is the weighted number density of galaxies in the redshift bin being correlated, and ω is the total area over which the correlations are calculated. Equation 15 describes the root mean square error due to intrinsic ellipticities.

Results

The resulting correlation functions for each redshift bin are shown in Figure 6 in addition to functions fitted using the curve_fit function provided in scipy's optimize module. Perhaps the most striking feature of these results is the sharp increase in ξ_+ for small angular separations, particularly for separations smaller than around 0.1 degrees.

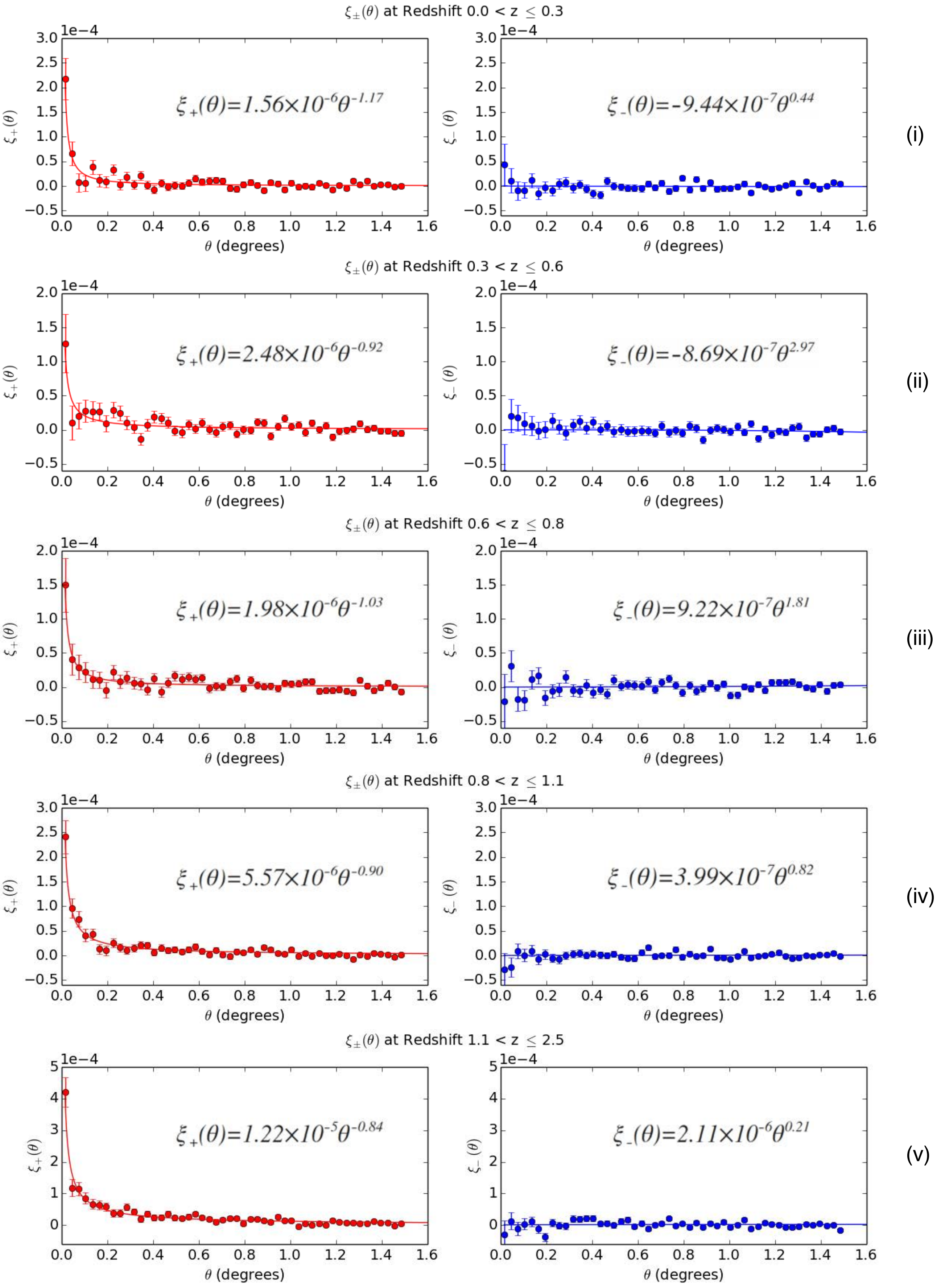

Figure 6: Two-point correlation functions, $\xi_{\pm}(\theta)$, calculated within five different redshift bins using the methods described above. Each resulting data set was fitted to a power law function with two free parameters using the curve_fit function provided by scipy. Individual data points are listed in Table C1. $\xi_+(\theta)$ exhibits a consistent excess for angular separations smaller than about 0.1 degrees while $\xi_-(\theta)$ is approximately zero at all separations.

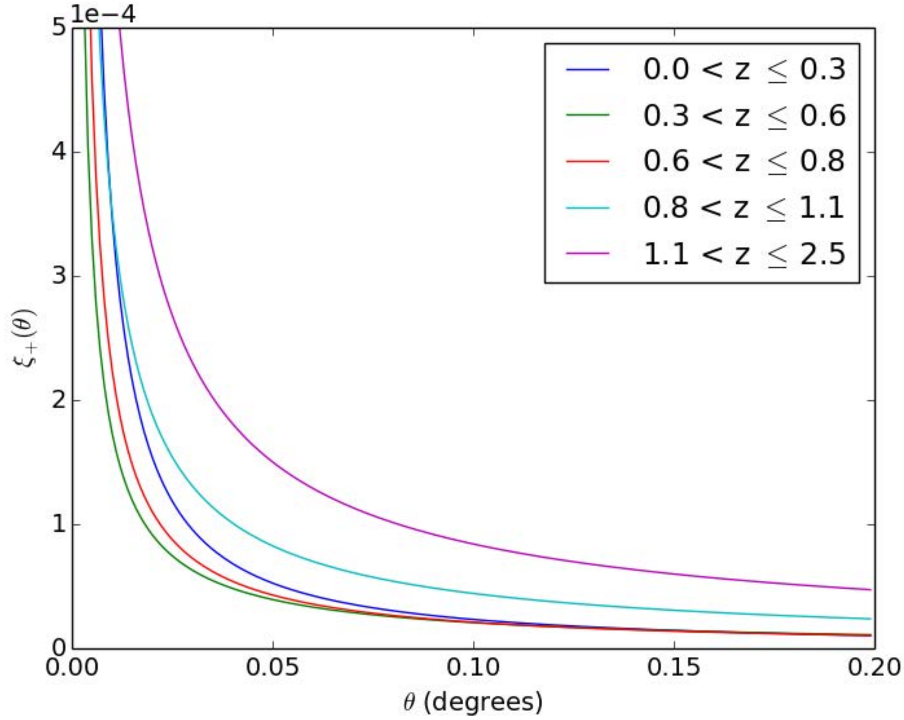

Figure 7: The trend lines shown in Figure 6 are displayed together. The magnitudes of the functions increase with redshift except in the case of the nearest redshift bin. This may be due to poor photometric redshift estimation in this region.

In addition, note that the excess correlation in the region near θ = 0.015 degrees is consistently of order 10^{-4}. This confirms our assumption that the shear component, γ, is much smaller than the intrinsic ellipticity, ϵ_0, for the large majority of the galaxies used in correlation (see Equation 4). Thus our use of Equation 3 in deriving the correlation functions has been validated. While ξ_+ shows a significant excess for angular separations close to zero, ξ_- shows no such excess. Instead it is consistent with zero for all angular separations less than 1.5 degrees. In other words, on average the excess shear in the direction tangential to the circle defined by a pair of galaxies is approximately equal in magnitude to the excess shear in the radial direction at all angular separations.

These results are in agreement with previous studies of weak lensing by large scale structure in the CFHTLS fields as well as with theoretical predictions of the correlation functions. Fu et al. (2008) measure the correlation functions in the CFHTLS Wide fields, and Van Waerbeke et al. (2000) measure the correlation functions in other fields observed by the Canada France Hawaii Telescope. Fu et al. report an excess correlation ξ_+ of order 10^{-4} for angular separations of about one arcminute, or 0.017 degrees, with the function quickly dropping off as the angular separation increases. In addition, Van Waerbeke et al. report an excess in ξ_+ of order 10^{-4} at angular separation approximately 0.02 degrees. We measured values of ξ_+ between $1x10^{-4}$ and $5x10^{-4}$ for separations $0.0 < \theta < 0.03$, which agrees with the results of Van Waerbeke et al. Van Waerbeke et al. also found $\langle \epsilon_t \ \epsilon_t \rangle$ and $\langle \epsilon_x \ \epsilon_x \rangle$ to have a similar shape and magnitude for angular separations around 0.02 degrees, resulting in a flat, nearly zero ξ_- function. This too agrees with our findings.

Miralda-Escudé (1991) presents predicted correlation functions given several different models including a cold dark matter model with $\Omega = 1$ and 50 km s^{-1} Mpc^{-1}. These theoretical predictions also agree with our results for the most part with ξ_+ exhibiting an excess at small angular separations of order 10^{-4} and ξ_- approximately zero for all separations. Miralda-Escudé also finds that the magnitude of the excess correlation is predicted to increase as redshift increases. While this trend is exhibited by the correlation functions we measure for redshift bins between z = 0.3 and z = 2.5, the nearest redshift bin, $0.0 < z < 0.3$, has a larger excess correlation than the redshift bins with redshift $0.3 < z < 0.8$. This result can be seen clearly in Figure 7, which shows the power law functions that were fitted to each correlation function. It is probable that the large correlation observed in the nearest redshift bin is a result of inaccurate binning due to the large redshift likelihood width exhibited by galaxies with reported photometric redshift less than 0.3. This bin is very likely to contain a significant number of galaxies with redshifts between 2.0 and 3.0 (see Figure A1 in Appendix A). In addition, Hildebrandt et al. (2012) report that the estimated photometric redshifts are well understood in the region $0.1 < z < 1.3$. Therefore, the significant number of galaxies in the nearest redshift bin with estimated redshifts of around 0.1 and lower contaminate the correlation functions calculated in this region. The width of the most distant redshift bin and the quick drop in the galaxy distribution for redshifts greater than 1.3 help to prevent a similar level of contamination in the most distant redshift bin, $1.1 < z < 2.5$.

Finally, for redshifts greater than 0.8, we detect a small nonzero excess correlation for angular separations up to about one degree. This is difficult to observe in Figure 6, but can easily be seen in Table C1 in Appendix C. This nonzero correlation indicates the detection of over-densities on degree scales.

Conclusion

We present two-point correlation functions, $\xi_{\pm}(\theta)$, calculated across CFHTLenS Wide fields W1, W2, W3, and W4 within five redshift bins of varying width. We found a consistent excess ξ_{+} correlation of order 10^{-4} at angular separations of around 0.015 degrees which quickly decreases for larger separations. For redshifts greater than 0.8, we find that the correlation exhibits a small nonzero excess for separations up to about one degree, indicating the detection of structure at those scales. The measured excesses increase as redshift increases, with the exception of a large excess measured for galaxies with redshift less than 0.3, which contradicts previous predictions and is likely due to poor redshift estimation in that region. In addition, we found that ξ_{-} is approximately zero for all redshift bins. With the exception of the large excess measured for very low redshift galaxies, these results are qualitatively consistent with previous studies and theoretical predictions, including a study which correlated the same fields.

Given the area covered by the fields correlated and the qualitative agreement with previous research, our results for redshifts larger than $z = 0.3$ may be robust enough to be used for cosmological purposes such as constraining the values of Ω_m and σ_8 or mapping dark matter distributions. However, a more quantitatively rigorous analysis of the results as well as error due to redshift binning and factors such as PSF corrections would be necessary. Moving forward, more area could be correlated by making use of additional surveys, objects could be cross-correlated between redshift bins in order to decrease error, and cosmological parameters could be constrained using the results presented here. In addition, using larger redshift bins would provide more accurate correlation functions, although it would result in a major increase in computing time as well as a lower resolution with regards to the time evolution of large-scale structure. Finally, given the redshift contamination exhibited in our results, future studies should handle galaxies with low reported photometric redshift with care. Simply removing these objects from consideration may be the best option given the data available.

References

Benítez, N., 1999, ASP Conference Series, 191, 31

Benjamin, J., Van Waerbeke, L., Heymans, C., et al., 2012, MNRAS, 431, 1575

Clowe, D., Gonzalez, A., Markevitch, M., 2004, APJ, 604, 596

Erben, T., Hildebrandt, H., Miller, L., et al., 2012, MNRAS, 433, 2545

Fu, L., Sembolini, E., Hoekstra, H., et al., 2008, arXiv:0712.0884 [astro-ph]

Goranova, Y., Hudelot, P., Magnard, F., et al., 2009, “The CFHTLS T0006 Release.”

Heymans, C., Van Waerbeke, L., Miller, L., et al., 2012, MNRAS, 427, 146

Hildebrandt, H., 2012, CFHTLenS Catalogue Data Description, http://www.cadc-ccda.hia-iha.nrc-cnrc.gc.ca/community/CFHTLens/README_catalogs_release.txt

Hildebrandt, H., Erben, T., Kuijken, K., et al., 2012, MNRAS, 14, 1

Hoekstra, H., Yee, H.K.C., Gladders, M.D., 2002, APJ, 577, 595

Miller, L., Heymans, C., Kitching, T.D., et al., 2011, MNRAS, 429, 2858

Miralda-Escudé, J., 1991, APJ, 380, 1

Schneider, P., Van Waerbeke, L., Kilbinger, M., Mellier, Y., 2002, A&A, 396, 1

Sembolini, E., Schrabback, T., Van Waerbeke, L., Vafaei, S., Hartlap, J., Hilbert, S., 2011, MNRAS, 410, 143

Van Waerbeke, L., Mellier, Y., Erben, T., et al., 2000, 358, 30

Van Waerbeke, L., Benjamin, J., Erben, T., et al., 2012, MNRAS, 18, 1

Wittman, D., Jain, B., Clowe, D., Dell'Antonio, I.P., Mandelbaum, R., May, M., Takada, M., Tyson, A., Wang, S., Zentner, A., 2009, *LSST Science Book,* 2.0, 499

Wittman, D.M., Tyson, J.A., Dell'Antonio, I., Bernstein, G., 2000, Nature, 405, 143

Acknowledgements

This work is based on observations obtained with MegaPrime/MegaCam, a joint project of CFHT and CEA/DAPNIA, at the Canada-France-Hawaii Telescope (CFHT) which is operated by the National Research Council (NRC) of Canada, the Institut National des Sciences de l'Univers of the Centre National de la Recherche Scientifique (CNRS) of France, and the University of Hawaii. This research used the facilities of the Canadian Astronomy Data Centre operated by the National Research Council of Canada with the support of the Canadian Space Agency. CFHTLenS data processing was made possible thanks to significant computing support from the NSERC Research Tools and Instruments grant program.

I thank Professors Heymans and Van Waerbeke for their timely and very helpful responses to questions regarding the contents of the CFHTLenS data catalogues as well as for helping to resolve technical difficulties encountered while acquiring data.

Finally, I would like to thank Professor Dell'Antonio for guiding me and teaching me as this project has evolved over the past two years. With Professor Dell'Antonio's help, I have grown as a physicist, and I have discovered a field which gives me a profound sense of accomplishment and satisfaction.

Appendix A.

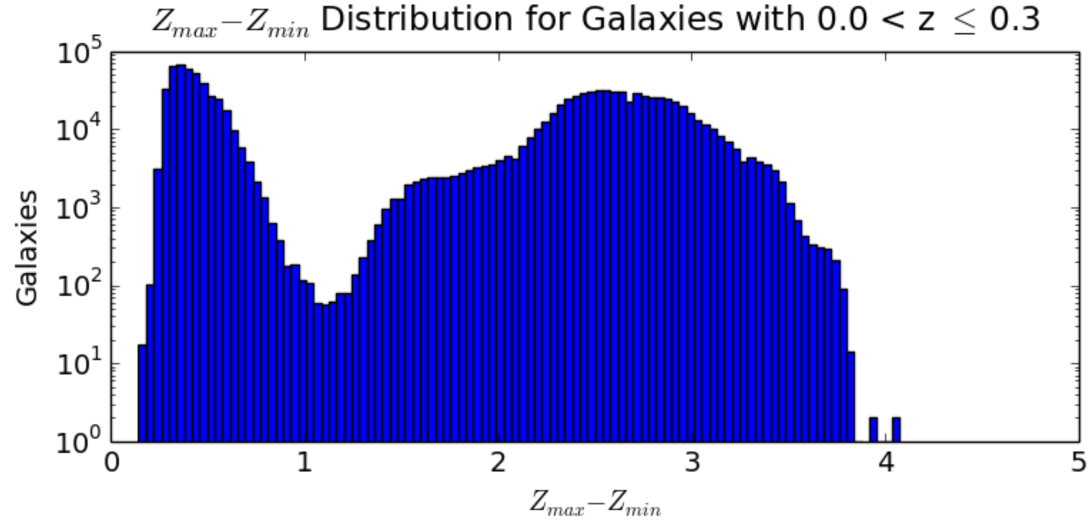

(i)

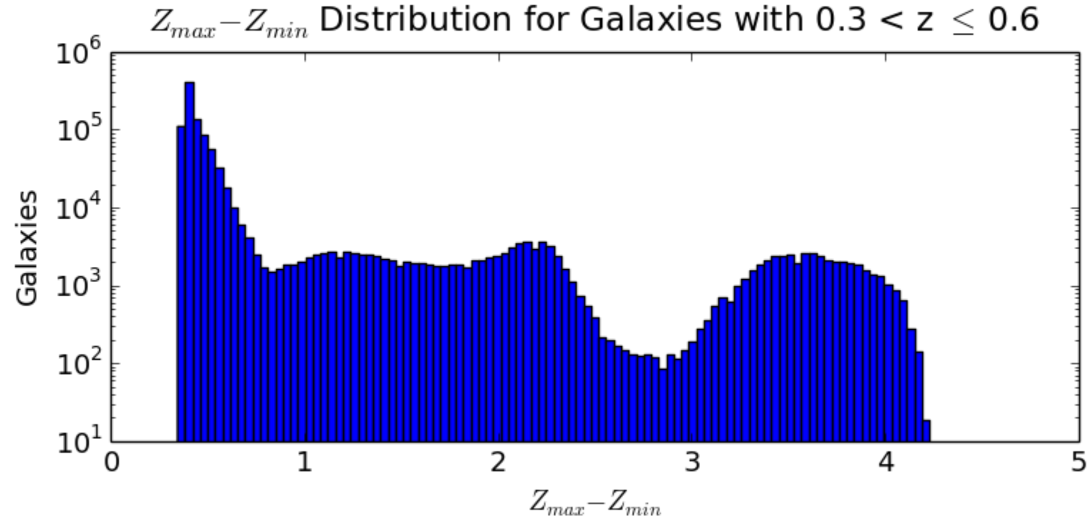

(ii)

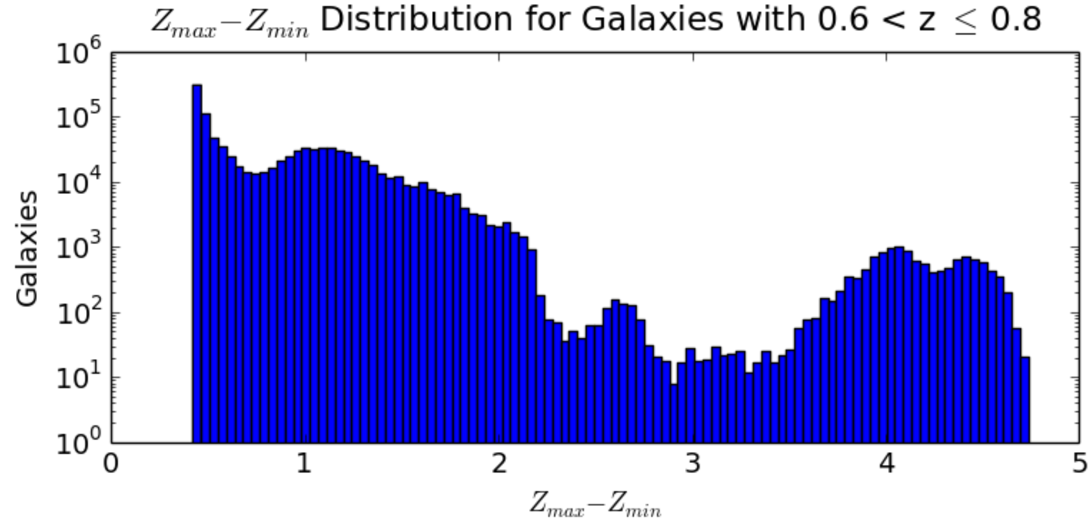

(iii)

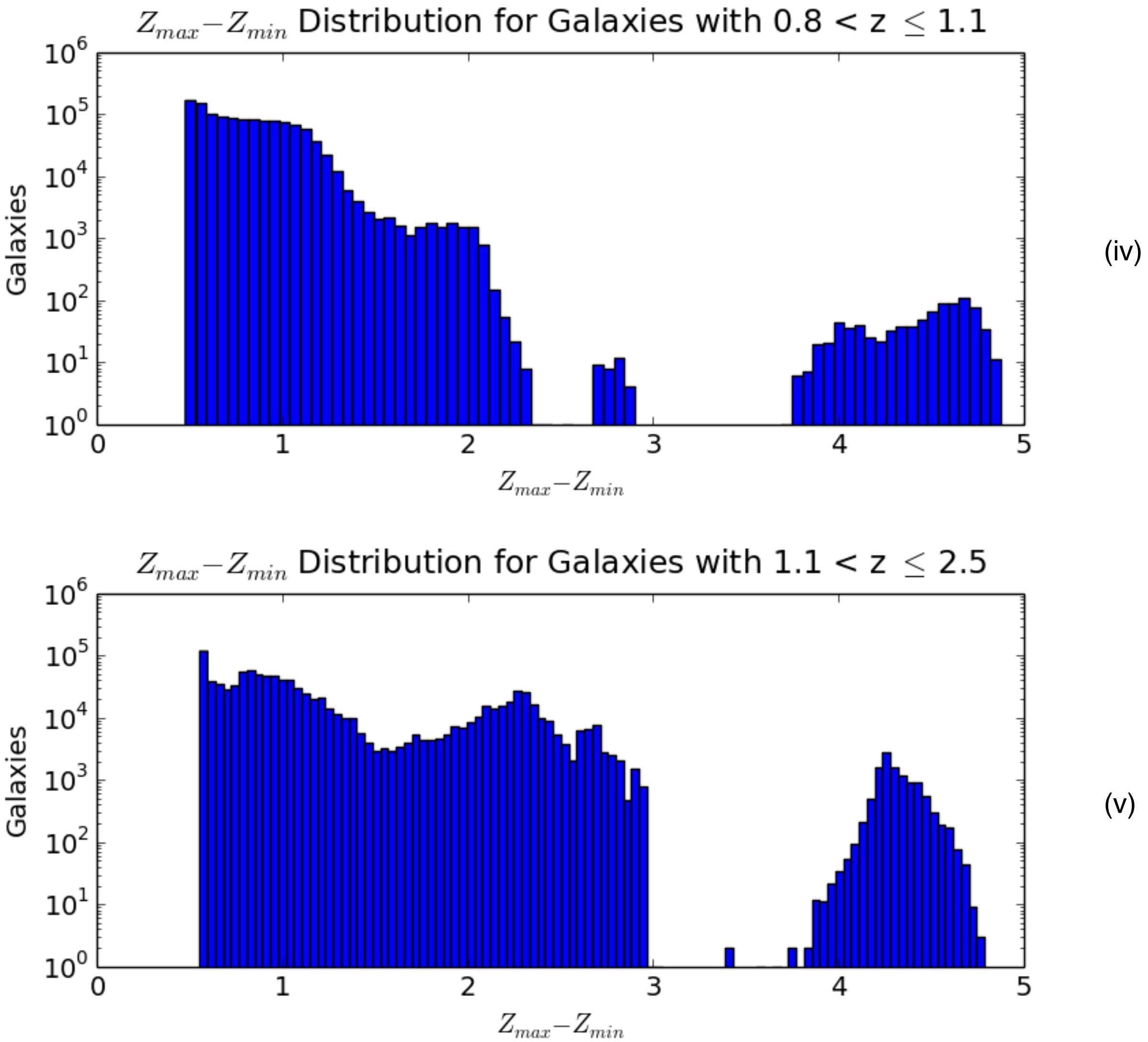

Figure A1: Distributions of the width of the Bayesian likelihood function used to estimate redshift. Distributions are calculated separately for each redshift bin to illustrate how the precision of the redshift estimates changes with redshift.

Appendix B.

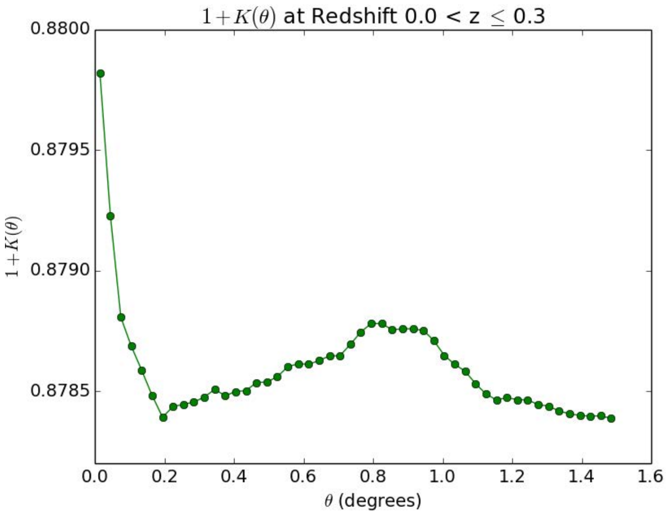

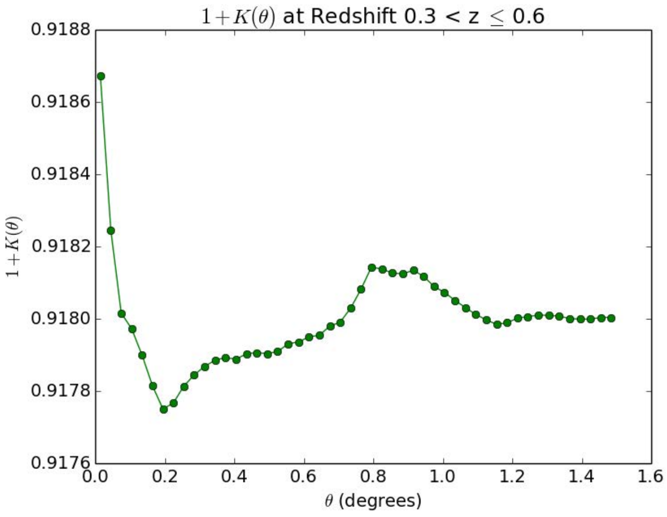

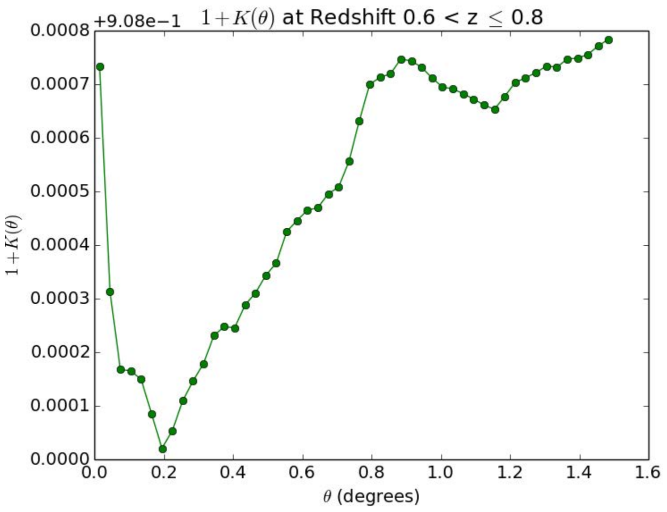

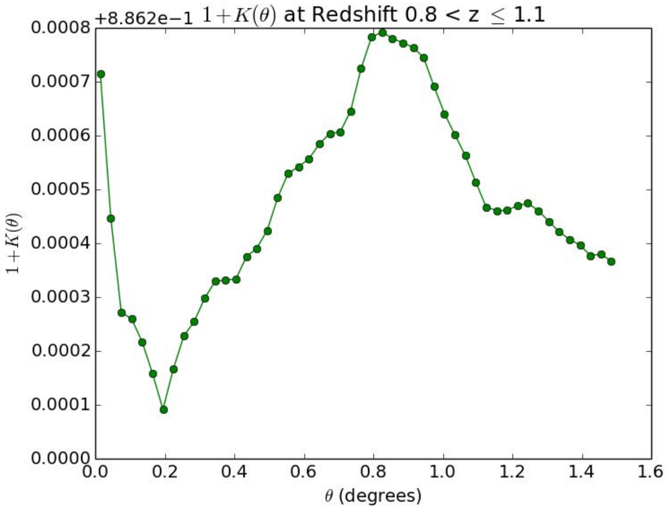

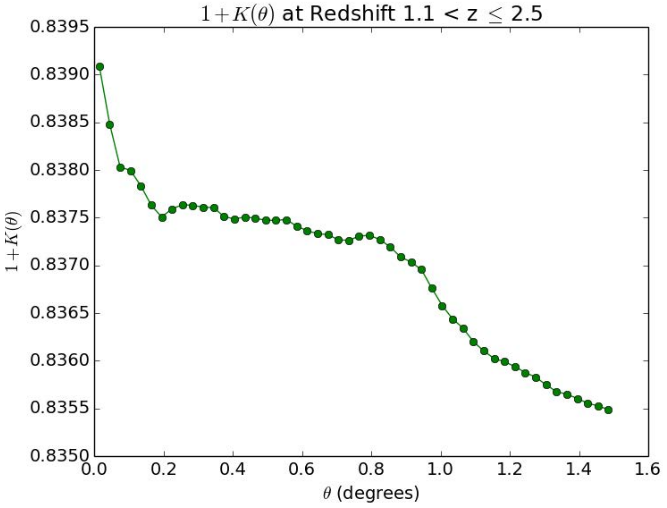

Figure B1: Calibration factors calculated in each redshift bin are shown for angular separations up to 1.5 degrees. Note that the calibration factor is small but significant with values ranging between 0.83 and 0.92. In addition, although 1+*K*(θ) varies with θ, the fluctuations are very small compared to the values of 1+*K*(θ). Thus the correlation functions are calibrated by an effectively constant factor within each redshift bin.

Appendix C.

	$0.0 < z \leq 0.3$		$0.3 < z \leq 0.6$		$0.6 < z \leq 0.8$		$0.8 < z \leq 1.1$		$1.1 < z \leq 2.5$	
θ	$\xi_+(\theta)$	$\xi_-(\theta)$	$\xi_+(\theta)$	$\xi_-(\theta)$	$\xi_+(\theta)$	$\xi_-(\theta)$	$\xi_+(\theta)$	$\xi_-(\theta)$	$\xi_+(\theta)$	$\xi_-(\theta)$
0.015	2.17E-04	4.37E-05	1.26E-04	-6.33E-05	1.50E-04	-2.05E-05	2.41E-04	-2.91E-05	4.21E-04	-3.03E-05
0.045	6.57E-05	1.12E-05	1.01E-05	2.05E-05	4.12E-05	3.12E-05	9.66E-05	-2.43E-05	1.18E-04	1.35E-05
0.075	6.93E-06	-9.20E-06	2.07E-05	1.76E-05	2.94E-05	-1.74E-05	7.42E-05	8.85E-06	1.15E-04	-1.07E-05
0.105	5.78E-06	-8.28E-06	2.74E-05	9.78E-06	2.19E-05	-1.92E-05	4.09E-05	2.51E-07	8.55E-05	4.12E-06
0.135	3.83E-05	1.14E-05	2.71E-05	6.45E-06	1.14E-05	1.10E-05	4.33E-05	9.36E-06	6.65E-05	1.15E-05
0.165	1.14E-05	-1.50E-05	2.72E-05	-9.63E-07	1.08E-05	1.72E-05	1.28E-05	-7.44E-06	6.35E-05	-1.07E-05
0.195	8.34E-06	-2.41E-06	9.44E-06	2.87E-07	-4.27E-06	-1.54E-05	9.90E-06	2.67E-06	5.87E-05	-3.68E-05
0.225	3.29E-05	-8.79E-06	2.92E-05	1.37E-05	2.21E-05	-5.89E-06	2.59E-05	-5.32E-06	3.87E-05	6.84E-06
0.255	2.78E-06	4.18E-06	2.45E-05	4.27E-06	8.39E-06	-3.36E-06	1.63E-05	-7.83E-06	3.77E-05	-9.93E-07
0.285	1.83E-05	7.65E-06	1.09E-05	-4.26E-06	1.40E-05	1.52E-05	1.04E-05	-2.94E-07	5.71E-05	-2.26E-06
0.315	3.53E-06	-3.66E-06	4.09E-06	6.72E-06	5.71E-06	-4.68E-06	1.46E-05	2.56E-06	4.23E-05	1.98E-05
0.345	2.12E-05	3.67E-06	-1.35E-05	1.21E-05	4.60E-06	-6.12E-06	2.11E-05	4.38E-06	2.01E-05	1.87E-05
0.375	2.21E-06	-5.69E-06	7.40E-06	2.74E-06	-3.20E-06	3.31E-06	2.04E-05	6.60E-07	3.51E-05	2.14E-05
0.405	-7.30E-06	-1.57E-05	1.90E-05	1.13E-05	1.22E-05	-7.86E-06	5.81E-06	3.65E-06	2.34E-05	2.14E-05
0.435	6.30E-06	-1.77E-05	1.70E-05	1.02E-06	-7.14E-06	-3.22E-06	1.57E-05	7.80E-07	2.48E-05	4.21E-06
0.465	-1.03E-06	1.09E-05	1.09E-05	6.16E-06	6.39E-06	-9.77E-06	1.01E-05	5.32E-07	3.62E-05	6.11E-06
0.495	1.19E-06	-4.92E-07	-9.99E-07	-2.19E-06	1.65E-05	1.08E-05	1.15E-05	3.26E-06	2.38E-05	2.16E-07
0.525	5.47E-07	-2.10E-06	-3.73E-06	5.12E-07	1.20E-05	1.44E-06	8.09E-06	-3.69E-06	2.20E-05	1.34E-05
0.555	6.61E-06	-4.09E-06	7.82E-06	-2.56E-06	1.52E-05	3.74E-06	1.22E-05	-5.53E-06	2.75E-05	1.81E-05
0.585	1.52E-05	-4.37E-06	1.77E-06	-1.86E-06	1.19E-05	3.13E-06	1.79E-05	-6.09E-06	3.64E-05	-3.21E-06
0.615	8.76E-06	-5.07E-06	1.04E-05	-9.74E-07	1.34E-05	2.10E-06	8.84E-06	6.68E-06	2.31E-05	6.41E-06
0.645	1.11E-05	4.78E-06	5.58E-07	-1.33E-06	-1.61E-06	8.31E-06	1.93E-06	1.61E-05	1.84E-05	-1.01E-05
0.675	1.23E-05	-3.08E-06	-3.27E-06	-4.21E-06	1.44E-06	-3.16E-06	1.09E-05	-1.82E-06	1.08E-05	1.51E-06
0.705	9.98E-06	5.48E-06	4.78E-06	6.21E-06	7.20E-07	6.74E-06	1.63E-06	-2.05E-07	1.77E-05	5.25E-06
0.735	-3.98E-06	-1.08E-05	6.71E-06	-3.98E-06	8.41E-06	1.27E-05	-1.92E-06	5.61E-07	2.12E-05	2.07E-05
0.765	-5.54E-06	-4.98E-06	-5.54E-06	-7.50E-07	1.28E-05	2.47E-06	7.99E-06	1.26E-05	2.27E-05	-8.23E-07
0.795	3.18E-06	1.59E-05	4.77E-07	-4.64E-06	-1.92E-06	-8.15E-06	6.51E-06	-3.63E-06	5.33E-06	4.19E-06
0.825	7.38E-06	-7.78E-06	-5.75E-07	6.34E-06	1.07E-05	2.48E-06	1.14E-05	3.73E-06	2.00E-05	-6.81E-06
0.855	2.04E-06	1.39E-05	1.14E-05	2.30E-06	2.83E-06	-5.73E-06	3.57E-06	-1.06E-06	1.97E-05	8.52E-06
0.885	-8.71E-06	-4.56E-06	1.02E-05	-1.44E-05	1.09E-06	-1.68E-06	1.62E-05	-4.37E-07	1.37E-05	-5.23E-06
0.915	7.17E-06	6.86E-06	-9.04E-06	-3.74E-07	1.46E-06	5.71E-06	1.17E-05	1.42E-05	1.00E-05	5.51E-06
0.945	5.06E-06	-6.61E-06	4.60E-06	3.06E-06	-1.81E-06	-7.84E-07	4.10E-06	-4.96E-06	2.68E-05	-1.31E-06
0.975	-7.40E-06	-4.89E-06	1.73E-05	7.86E-07	5.99E-06	4.93E-06	3.43E-06	-4.92E-06	1.54E-05	1.10E-05
1.005	6.46E-06	-5.25E-06	5.20E-06	-2.26E-06	4.71E-06	-1.19E-05	1.25E-05	-7.67E-06	1.37E-05	-6.71E-06
1.035	-2.15E-06	-1.22E-06	7.60E-06	4.85E-06	5.25E-06	-1.14E-05	-1.58E-06	-7.87E-07	-3.67E-06	9.69E-07
1.065	3.27E-07	5.01E-06	-3.68E-06	-3.41E-06	8.31E-06	5.76E-07	4.69E-06	8.38E-06	4.65E-06	1.74E-05
1.095	-2.21E-06	-1.36E-05	1.01E-05	8.81E-06	8.40E-06	-2.21E-06	-9.45E-07	-4.13E-06	6.91E-07	-1.05E-05
1.125	5.88E-06	2.47E-06	2.15E-07	-1.28E-05	-6.06E-06	3.96E-06	4.20E-06	-1.75E-06	4.65E-06	-2.86E-06
1.155	1.18E-06	-1.58E-06	6.46E-06	1.74E-06	-4.73E-06	-4.23E-06	7.22E-07	2.43E-07	1.55E-06	6.77E-06
1.185	-7.50E-06	-6.02E-06	-1.07E-05	-7.44E-06	-4.39E-06	7.16E-06	-1.21E-07	2.40E-06	1.55E-05	4.09E-06
1.215	1.17E-06	-2.49E-06	-1.89E-06	-1.72E-06	-4.13E-06	7.45E-06	3.15E-06	6.01E-06	1.01E-05	1.43E-06
1.245	-4.70E-06	1.30E-06	-8.75E-07	-3.39E-06	-5.91E-06	7.51E-06	-1.04E-07	-1.20E-06	6.77E-06	-5.95E-06
1.275	1.11E-05	5.63E-06	1.41E-06	3.07E-06	-7.58E-06	7.95E-06	-8.17E-06	-6.70E-06	7.33E-06	-7.35E-06
1.305	2.25E-06	-1.33E-05	9.28E-06	5.34E-06	9.99E-06	4.23E-06	1.05E-06	-4.95E-06	5.56E-06	-5.13E-06
1.335	1.11E-05	9.53E-06	1.02E-06	-1.16E-05	2.01E-06	-8.25E-07	-1.21E-06	-5.89E-07	5.97E-06	4.10E-06
1.365	-6.41E-07	1.36E-06	2.76E-06	-5.83E-06	-5.28E-06	-2.42E-06	4.69E-06	-1.20E-06	1.26E-05	1.24E-06
1.395	2.25E-06	-6.22E-06	-1.25E-06	-6.10E-06	-5.98E-07	3.70E-06	2.94E-06	2.06E-06	7.13E-06	4.86E-06
1.425	3.59E-06	-1.14E-07	-1.54E-06	2.83E-07	6.01E-06	-5.85E-06	1.87E-06	1.02E-06	7.29E-06	-2.44E-06
1.455	-1.50E-06	7.92E-06	-4.47E-06	3.19E-06	3.88E-07	2.87E-06	-3.52E-06	5.19E-06	-1.43E-06	4.43E-07
1.485	4.60E-08	5.15E-06	-4.67E-06	-2.63E-06	-6.60E-06	3.72E-06	1.80E-06	-1.74E-06	5.45E-06	-1.49E-05

Table C1: Individual data points of the correlation functions shown in Figure 6. Note that the values of the functions are determined by averaging over pairs separated by angle $\theta \pm 0.015$ degrees.

Appendix D.

This is an example of the Python code used to create correlations within an individual field. In particular, this example produces $\xi_{\pm}(\theta)$ for each redshift bin in W2. By simply replacing references to W2 in this script with other fields and combining the results of all scripts, the correlation functions across multiple fields were produced.

```
from math import *
import pickle
import multiprocessing as mp

# Set constant index values for more flexibility
RA = 0
DEC = 1
SMAJOR = 2
SMINOR = 3
THETA = 4
ERRA = 5
ERRB = 6
ERRTHETA = 7
E1 = 8
E2 = 9
WEIGHT = 10
Z = 11
ZMIN = 12
ZMAX = 13
M = 14
C2 = 15

MAXR = 1.5
RBINS = 50
DELTAR = MAXR/RBINS

layers = 5
maxz = 2.5
allXiData = [[[0.0, 0.0, 0.0] for i in range(RBINS)] for j in range(layers)]

# Parse the input file.
inputFile = open('/home/pike/input/WeightedCFHTLensW2.tsv', 'r')
objects = []
for line in inputFile:
    splitLine = line.split('\t')
    if 0.0<=float(splitLine[Z])<=maxz:
            objects.append(map(float, splitLine[:-1]))
```

```
inputFile.close()

# Split galaxies into redshift bins.
layeredObjects = [[]for i in range(layers)]
for x in objects:
    if x[Z] <= 0.3:
        layeredObjects[0].append(x)
    elif x[Z] <= 0.6:
        layeredObjects[1].append(x)
    elif x[Z] <= 0.8:
        layeredObjects[2].append(x)
    elif x[Z] <= 1.1:
        layeredObjects[3].append(x)
    else:
        layeredObjects[4].append(x)

del objects

# Compares objects in the W2 field. Uses the eq. given by Heymans et al 2012
def compare(a):
    depth = a[0]
    modclass = a[1]         # A number passed when called inside pool.map().
Each process
    numcpus = a[2]          # iterates over galaxies with index modclass mod
numcpus and
    zbin = layeredObjects[depth]    #compares them to every galaxy with a
larger index.
    xiPlus = [0.0 for i in range(RBINS)]
    xiMinus = [0.0 for i in range(RBINS)]
    Ktheta = [0.0 for i in range(RBINS)]
    currindex = modclass
    zbinlen = len(zbin)
    while currindex<zbinlen:
        x = zbin[currindex]
        for j in range(currindex+1, zbinlen):
            y = zbin[j]
            radif = radians(x[RA]-y[RA])
            r =
degrees(acos((cos(radif)*cos(radians(x[DEC]))*cos(radians(y[DEC]))) +\
(sin(radians(x[DEC]))*sin(radians(y[DEC])))))
            if r<MAXR:
                rbin = int(r/DELTAR)
            # Determine the angle of the rotated frame.
                thetaxy = atan((sin(radif)*cos(radians(y[DEC])))/ \
((cos(radians(x[DEC]))*sin(radians(y[DEC])))-\
                    (sin(radians(x[DEC]))*cos(radians(y[DEC]))*cos(radif))))
                xe1 = x[E1]
                xe2 = x[E2] - x[C2]
                ye1 = y[E1]
```

```
                ye2 = y[E2] - y[C2]
                xweight = x[WEIGHT]
                yweight = y[WEIGHT]
                xiPlus[rbin] += xweight*yweight*((xe1*ye1)+(xe2*ye2))
                xiMinus[rbin] += xweight*yweight*((((xe1*ye2)- \
(xe2*ye2))*cos(4*thetaxy))+(((xe1*ye2)+(xe2*ye2))*sin(4*thetaxy)))
                Ktheta[rbin] += xweight*yweight*(1.0+x[M])*(1.0+y[M])

        currindex += numcpus
    xiData = (xiPlus, xiMinus, Ktheta)
    return xiData

# Make a pool of workers to split up the task. Each worker gets a number
between 0 (inclusive) and the number of available # cpus (exclusive).
pool = mp.Pool()
cpus = mp.cpu_count()
for i in range(layers):
    print(i)
    zeta = pool.map(compare,[[i,j,cpus] for j in range(cpus)])
    for x in zeta:
        for j in range(RBINS):
            allXiData[i][j][0] += x[0][j]
            allXiData[i][j][1] += x[1][j]
            allXiData[i][j][2] += x[2][j]
del pool
# Dump and apply multiplicative calibrations:
xiPlusArray = [[(allXiData[i][j][0]/allXiData[i][j][2]) for j in
range(RBINS)] for i in range(layers)]
xiMinusArray = [[(allXiData[i][j][1]/allXiData[i][j][2]) for j in
range(RBINS)] for i in range(layers)]
KthetaArray = [[allXiData[i][j][2] for j in range(RBINS)] for i in
range(layers)]
outputPlus = open('/home/pike/output/CFHTLensW2PlusDump.txt', 'w')
pickle.dump(xiPlusArray, outputPlus)
outputPlus.close()
outputMinus = open('/home/pike/output/CFHTLensW2MinusDump.txt', 'w')
pickle.dump(xiMinusArray, outputMinus)
outputMinus.close()
outputKtheta = open('/home/pike/output/CFHTLensW2KthetaDump.txt','w')
pickle.dump(KthetaArray, outputKtheta)
outputKtheta.close()
```